Projection angle dependence in grating-based X-ray dark-field imaging of ordered structures

Florian Bayer,[1,*] **Simon Zabler,**[2] **Christian Brendel,**[1]
Georg Pelzer,[1] **Jens Rieger,**[1] **André Ritter,**[1] **Thomas Weber,**[1]
Thilo Michel,[1] **and Gisela Anton**[1]

[1] *Erlangen Centre for Astroparticle Physics (ECAP), Friedrich-Alexander-Universität Erlangen-Nürnberg, Erwin-Rommel-Str 1, D-91058 Erlangen, Germany*
[2] *Chair of X-ray Microscopy, Universität Würzburg, Department of Physics, Am Hubland, D-97074 Würzburg, Germany*

[*]florian.l.bayer@fau.de

Abstract: Over the recent years X-ray differential phase-contrast imaging was developed for the hard X-ray regime as produced from laboratory X-ray sources. The technique uses a grating-based Talbot-Lau interferometer and was shown to yield image contrast gain, which makes it very interesting to the fields of medical imaging and non-destructive testing, respectively. In addition to X-ray attenuation contrast, the differential phase-contrast and dark-field images provide different structural information about a specimen. For the dark-field even at length scales much smaller than the spatial resolution of the imaging system. Physical interpretation of the dark-field information as present in radiographic and tomographic (CT) images requires a detailed look onto the geometric orientation between specimen and the setup. During phase-stepping the drop in intensity modulation, due to local scattering effects within the specimen is reproduced in the dark-field signal. This signal shows strong dependencies on micro-porosity and micro-fibers if these are numerous enough in the object. Since a grating-interferometer using a common unidirectional line grating is sensitive to X-ray scattering in one plane only, the dark-field image is influenced by the fiber orientations with respect to the grating bars, which can be exploited to obtain anisotropic structural information. With this contribution, we attempt to extend existing models for 2D projections to 3D data by analyzing dark-field contrast tomography of anisotropically structured materials such as carbon fiber reinforced carbon (CFRC).

© 2013 Optical Society of America

OCIS codes: (110.7440) X-ray imaging; (340.7450) X-ray interferometry; (110.6955) Tomographic imaging; (160.2290) Fiber materials; (110.3175) Interferometric imaging.

References and links

1. A. Momose, W. Yashiro, Y. Takeda, Y. Suzuki, and T. Hattori, "Phase Tomography by X-ray Talbot Interferometry for Biological Imaging," Japanese Journal of Applied Physics **45,** 5254–5262 (2006).
2. T. Weitkamp, A. Diaz, C. David, F. Pfeiffer, M. Stampanoni, P. Cloetens, and E. Ziegler, "X-ray phase imaging with a grating interferometer," Opt. Express **13,** 6296-304 (2005).
3. P. Cloetens, W. Ludwig, J. Baruchel, D. VanDyck, J. Van Landuyt, J.-P. Guigay, and M. Schlenker, "Holotomography: Quantitative phase tomography with micrometer resolution using hard synchrotron radiation x rays," Appl. Phys. Lett. **75,** 2912–14 (1999).

4. F. Bayer, K. Gödel, W. Haas, J. Rieger, A. Ritter, T. Weber, L. Wucherer, J. Durst, T. Michel, and G. Anton, "Spectroscopic dark-field imaging using a grating-based Talbot-Lau interferometer," in *Physics of Medical Imaging*, Proc. SPIE **8313,** 83135 (2012).

5. F. Pfeiffer, M. Bech, O. Bunk, P. Kraft, E. F. Eikenberry, C. Brönnimann, C. Grünzweig, and C. David, "Hard-X-ray dark-field imaging using a grating interferometer," Nature materials **7,** 134-137 (2008).

6. H. Wen, E. Bennett, M. Hegedus, and S. Carroll, "Spatial harmonic imaging of X-ray scatteringInitial Results," IEEE Trans. Med. Imaging **27,** 997–1002 (2008).

7. V. Revol, I. Jerjen, C. Kottler, P. Schütz, R. Kaufmann, T. Lüthi, U. Sennhauser, U. Straumann, and C. Urban, "Sub-pixel porosity revealed by x-ray scatter dark field imaging," J. Appl. Phys. **110,** 044912 (2011).

8. W. Yashiro, Y. Terui, K. Kawabata, and A. Momose, "On the origin of visibility contrast in x-ray Talbot interferometry," Opt. Express **18,** 16890–901 (2010).

9. V. Revol, C. Kottler, R. Kaufmann, A. Neels, and A. Dommann, "Orientation-selective X-ray dark field imaging of ordered systems," J. Appl. Phys. **112,** 114903 (2012).

10. M. Bech, O. Bunk, T. Donath, R. Feidenhans'l, C. David, and F. Pfeiffer, "Quantitative x-ray dark-field computed tomography," Phys. Med. Biol. **55,** 5529-39 (2010).

11. T. H. Jensen, M. Bech, O. Bunk, T. Donath, C. David, R. Feidenhans'l, and F. Pfeiffer, "Directional x-ray dark-field imaging," Phys. Med. Biol. **55,** 3317-3323 (2010).

12. H. Wen, E. Bennett, M. Hegedus, and S. Rapacci, "Fourier X-ray scattering radiography yields bone structural information," Radiology **252,** 910–918 (2009).

13. G. Potdevin, A. Malecki, T. Biernath, M. Bech, T. H. Jensen, R. Feidenhans'l, I. Zanette, T. Weitkamp, J. Kenntner, J. Mohr, P. Roschger, M. Kerschnitzki, W. Wagermaier, K. Klaushofer, P. Fratzl, and F. Pfeiffer, "X-ray vector radiography for bone micro-architecture diagnostics," Phys. Med. Biol. **57,** 3451-3461 (2012).

14. T. Jensen, M. Bech, I. Zanette, T. Weitkamp, C. David, H. Deyhle, S. Rutishauser, E. Reznikova, J. Mohr, R. Feidenhans'l, and F. Pfeiffer, "Directional x-ray dark-field imaging of strongly ordered systems," Phys. Rev. B **82,** 214103 (2010).

15. E. Reznikova, J. Mohr, M. Boerner, V. Nazmov, and P.-J. Jakobs, "Soft X-ray lithography of high aspect ratio SU8 submicron structures," Microsyst. Technol. **14,** 1683-1688 (2008).

16. J.-P. Guigay, S. Zabler, P. Cloetens, C. David, R. Mokso, and M. Schlenker, "The partial Talbot effect and its use in measuring the coherence of synchrotron X-rays," J. Syncrotron Rad. **11,** 476–482 (2004).

17. V. Revol, C. Kottler, R. Kaufmann, F. Cardot, P. Niedermann, I. Jerjen, T. Lüthi, U. Sennhauser, U. Straumann, and C. Urban, "Sensing Small Angle Scattering with an X-ray Grating Interferometer," in *Proceedings of IEEE Nuclear Science Symposium and Medical Imaging Conference* (Institute of Electrical and Electronics Engineers, New York, 2010), pp. 892–895.

1. Introduction

The X-ray Talbot-Lau interferometer has become an important tool over the past decade for its ability to record differential phase-contrast (DPC) images by using spatially incoherent laboratory X-ray sources in combination with line gratings which encode the differential phase of the wave field and hence of the object transmission function [1, 2]. This relatively new method has to be considered a complementary technique to inline phase-contrast imaging which is used to numerically retrieve the phase-map from Fresnel-propagated radiographs [3]. Compared to the latter method, which needs high image resolution, DPC images are recorded in the laboratory at low magnifications and pixels of 50 microns size or more. Consequently, larger objects can be imaged in 2D and 3D phase imaging. Yet, details which are smaller than the pixel sampling are not imaged directly.

The information, which today is retrieved from DPC images is threefold and is extracted in the form of three separate images: (a) The attenuation signal which corresponds to the line integrals of the material's linear absorption coefficient; (b) The differential phase-contrast which can be integrated to an image of the phase gradient, which is the refractive index or electron density gradient; (c) The visibility or so-called scattering or dark-field contrast (DFC), that is linked to the integrated scattering power of the investigated specimen. The latter has been identified to encode sub-sampling structural details in the visibility of the signal, whereby visibility shows a decrease when passing through the scatter media [4–7]. This scattering is mostly elastic and originates from microscopic inhomogeneities, which are smaller than the pixel size. It corresponds to ultra-small-angle X-ray scattering [8,9] and predominantly does not relate to ab-

sorption effects. When this scattering effect is isotropic the images can be reconstructed into a 3D volume representing a qualitative scattering density [10]. Yet, when the scattering medium is anisotropic, as it is the case e.g. for nonisotropically aligned fibrous collocations such as fiber-reinforced composites or naturally structured material like bone or wood, the scattering image depends on the orientation of the fibers with respect to the Talbot gratings [11,12]. Directional information on samples with ordered micro-structures can therefore be exploited using DFC imaging [13,14]. Yet, no attempts have been made so far to reconstruct such data to a 3D volume. As for the visibility modulations (i.e., DFC), when rotating an anisotropically scattering sample around the X-ray beam axis, these are well understood and described by analytical models [14]. While the influence of the polar angle θ with respect to the grating lines (see Fig. 1 for the definition of the angles) is sufficient to describe the DFC signal of flat fibrous samples, the DFC signal dependence on the azimuthal angle ϕ, which corresponds to the projection angle in a tomographic scan, has not been fully described yet. Since the DFC is influenced by the local fiber orientation within a three-dimensional bulk sample [8], a single 2D projection onto the grating plane, perpendicular to the X-ray beam, does not allow to observe the local orientation. With this work we present measurements of a bundle of carbon fibers whose orientation is varied in order to cover the full range of the coordinate angles θ and ϕ. Such a study is essential to be able to explore the full 3D angular information of fibrous structures and to obtain anisotropic microstructural information such as orientation, degree of alignment or quality of layering, which gives a completely new observable information in X-ray imaging. In order to illustrate the potential of such measurements we present a DFC tomography of a carbon fiber reinforced carbon (CFRC) sample.

2. Materials and Methods

The laboratory setup is schematized in Fig. 1. It corresponds to a Talbot-Lau grating interferometer setup, very similar to the original design by Weitkamp et al. [2].
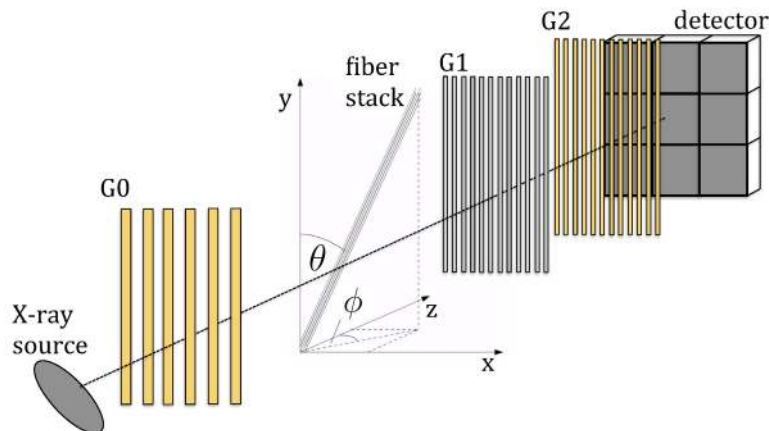

Fig. 1. Sketch of the Talbot-Lau interferometer setup. The investigated test sample, for this case a parallel aligned fiber stack, is placed in front of the phase-grating G1. The definition of the coordinate angles θ and ϕ is shown.

The polychromatic X-ray spectrum produced by a commercial rotating anode tube (ME-GALIX CatPlus 125/40/90, Siemens AG, Erlangen, Germany) was used to illuminate the gratings. These were manufactured by the Institute for micro-structure technology at the Karlsruhe Institute of Technology (KIT) using the so-called LIGA process [15]. The Talbot-Lau interfer-

ometer comprises three gratings: The first grating G0 is a "source-grating" defining the necessary horizontal spatial coherence, as required for the phase- (G1) and the analyzer-grating (G2). The height of the phase-grating's bars in z-direction is $h_1 = 8.7\,\mu$m, and was chosen to superimpose phase shifts of π onto an incoming plane wave of 25 keV (the so-called design energy). According to the Talbot effect, the periodic structures of G1, when coherently illuminated with a plane wave, reproduce in terms of complex intensity patterns, when the wave propagation length is equal to multiples of the so-called Talbot distance $d_T = \frac{2p_1^2}{\lambda_{design}}$, with p_1 the pitch of the G1 grating. For a π-shifting rectangular phase-grating, the intensity patterns show in particular a periodical intensity distribution with periodicity $\frac{p_1}{2}$ with locations of maximal interference at multiples of the fractional Talbot distance $\frac{p_1^2}{8\lambda_{design}}$. The analyzer-grating (G2) is placed in the third order Talbot distance $d_{3.TO}$ downstream of G1, using that so-called fractional Talbot effect [16]. The analyzer-grating G2 is made of gold bars with $p_2 = 2.4\,\mu$m pitch, whereas G1 is made of Nickel and features $p_1 = 4.37\,\mu$m pitch. Taking image magnification into account, the distance between G1 an G2 is $d_{3.TO}^* = 15.9$ cm. The source-grating G0 is also made from gold and has a pitch of $p_0 = 23.95\,\mu$m. Both absorption gratings G0 and G2 feature rectangular bars of $150\,\mu$m and $110\,\mu$m height, respectively. The sample is placed upstream of G1. DPC images are reconstructed from four phase steps of G2 over one period. Radiographs are recorded downstream of G2 with a Varian flat-panel detector (PaxScan 2520D, Varian Inc., USA), calibrated for the corresponding frame exposure time. Because of the limited area covered by the line gratings, the field of view (FOV) was restricted to 2 cm x 5 cm, i.e. 160 x 400 pixels (detector pixel size is $127\,\mu$m). In each pixel the intensity pattern of the phase-stepping measurement was fitted to a cosine according to

$$I(k) = a + b \cdot \cos\left(2\pi\frac{k\tau}{p_2} + \Phi\right) \tag{1}$$

Here, a is proportional to the beam attenuation and b is the amplitude of the phase-stepping curve. Φ encodes the local phase shift (modulo 2π), p_2 is the pitch of the analyzer-grating, whereby $\tau = 0.6\,\mu$m is the horizontal step size and k the integer step number (1, ..,4). The attenuation, DPC and DFC values are determined with respect to a bright-field reference (no sample in the beam) which is obtained by the same phase-stepping procedure. From the normalized visibility $V = \frac{b}{a}$ dark-field images are calculated as the ratio $\frac{V}{V_0}$ of the object visibility V and the bright-field visibility V_0, for every pixel of the detector matrix. Note, that for the Talbot-Lau interferometer used in this study, when illuminated with a 40 kVp tungsten spectrum and with a tube current of 60 mA, an average bright-field visibility of $V_0 = 22\%$ is achieved.
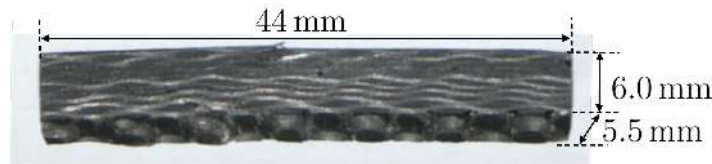

Fig. 2. Photography of the CFRC sample investigated in a dark-field computed tomography scan.

One of the investigated samples is a block of carbon fiber reinforced carbon (CFRC) with dimensions of $44\,\text{mm} \times 6.0\,\text{mm} \times 5.5\,\text{mm}$ (see Fig. 2). It contains woven fabric sheets of carbon fiber bundles of some tenth of millimeter length, embedded in a quasi-amorphous graphite matrix that ensures the cohesion between the fibers and layers. The test sample consists of layers with cross-woven bundles forming a rectangular pattern. These layers are stacked to a bulk

sample, whereas the preferential directions of the fibers in different layers vary: the fibers in top and bottom layers are orientated in x- and z-direction, whereby two intermediate layers are rotated by 45° around y-axis. The fiber volume fraction within the composite typically amounts to 50%. The sample is positioned in such a manner that all sheets lie in x-z-plane, perpendicular to the grating bars, see Fig. 1. Thereby maximum DFC variations are achieved, and a full axial CT scan is recorded for this sample, comprising 601 projections each retrieved from four exposures of 1.32 s per phase step. Together with waiting times for rotation and object movement between sample and reference measurement, the total scan time is 364 minutes, whereby reference images are taken every 25 projections. The X-ray tube is operated at 60 kVp and 25 mA current. For that tube spectrum a bright-field visibility of approx. 5% is achieved with
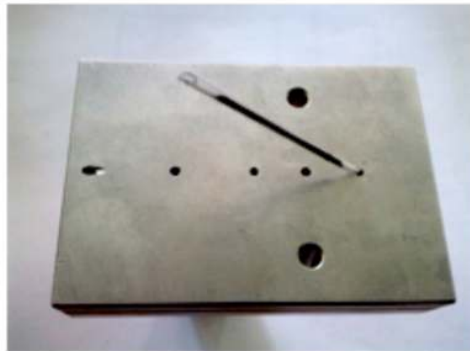

Fig. 3. Photography of the fiber sample in the holder: The glass capillary filled with the carbon fiber bundle can be mounted at different angles of elevation, i.e. $0°, 15°, 30°, 45°, 60°$. The holder is mounted onto a rotation axis which permits additional azimuthal rotation for CT imaging.
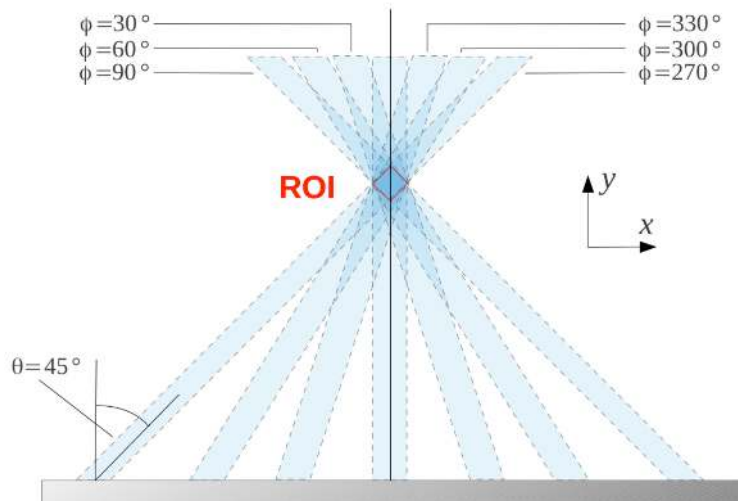

Fig. 4. Sketch of the stacked fiber bundle sample, showing azimuthal scanning positions for an elevation of $\theta = 45°$ for several azimuthal angles ϕ. The dark-field signal of the depicted ROI intersection was averaged for evaluation.

the given interferometer setup. In order to evaluate the DFC variations of aligned carbon fibers as a function of both the azimuthal and the elevation angle, we used a thin glass capillary (tip of a Pasteur pipette with 0.8 mm inner diameter and 0.35 mm walls) which was filled manually with a bundle of stacked carbon fibers, each fiber approx. 30 mm long and 7 μm in diameter. Figure 3 shows the sample holder with the filled glass capillary mounted at 30° elevation. Each hole in the holder plate allows for a different sample elevation with respect to the grating bars which are vertical, i.e. $\theta = 0°, 15°, 30°, 45°$ and 60°. For each elevation angle θ the sample was rotated axially around 360° and DPC images were taken at azimuthal steps every 18°. From the retrieved dark-field images the average normalized visibility was calculated in the central intersection of all sample positions (cf. ROI in Fig. 4). The integrated exposure time per phase step was 10 s. For each of the twenty object images a bright-field reference image was taken, which results in a total measurement time of 49 minutes for this test.

3. Results

3.1. CFRC sample

In a first step, the CFRC sample was examined. Figure 5 shows three dark-field projection images of three blocks of CFRC on top of each other in an axial scan (rotation axis is vertical, thus parallel to the grating bars), corresponding to (a) $\phi = 0°$, (b) $\phi = 41.4°$ and (c) $\phi = 66.6°$.
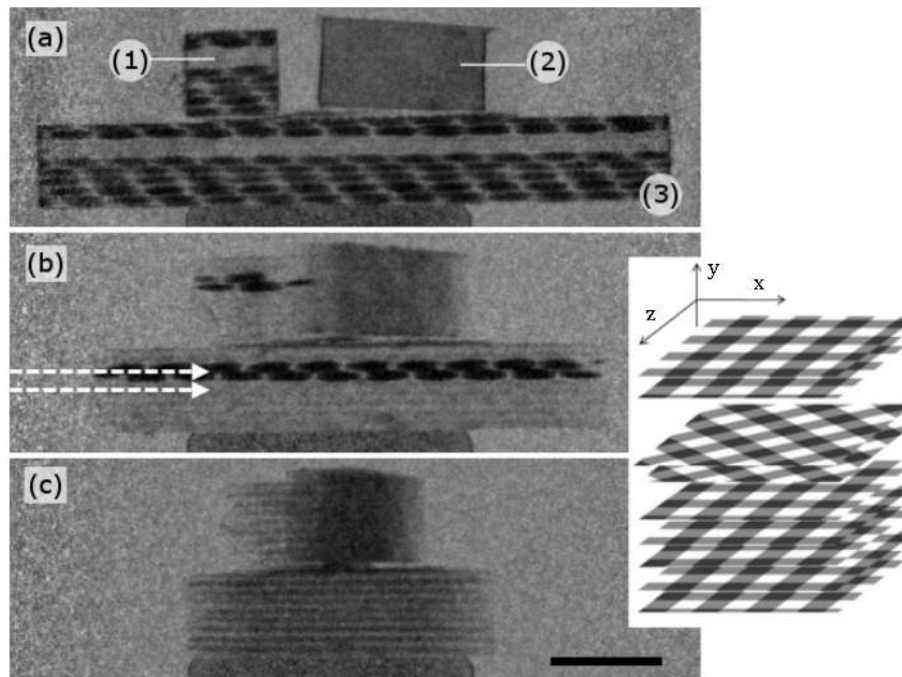

Fig. 5. Three representative DFC images from the CT scan of the CFRC sample in axial scan: $\phi = 0°$ (a), $\phi = 41.4°$ (b) and $\phi = 66.6°$ (c). The inset on the right side shows schematically the different orientations of the cross-woven fiber sheets in blocks (1) and (3) with respect to the coordinate axes defined in Fig. 1.

Dark image signal indicates strong X-ray scattering. The block (1) is a cubic piece of CFRC which consists of a sequence (from the bottom to the top) of five cross-woven horizontal sheets where the fiber orientations align with the cube's edges, then two cross-woven sheets which

are rotated 45° to the latter (hence the fibers diagonal to the cube's edges), followed by two sheets where again the fiber alignment is along the edges. The main axes of the structure (1) are labeled in the inset of Fig. 5. Block (2) has dimensions similar to (1) but is rotated 90° around axis x, hence the cross-woven sheets are no longer perpendicular to the grating bars. Block (3) is an elongated version of block (1) with the same orientation of the sheets. A photography of block (3) was shown in Fig. 2. The changes in DFC signal with the azimuthal angle ϕ are best observed in block (3). One can clearly see that most of the fiber bundle plies appear black due to strong scattering, some other bundles in two intermediate sheets white, at 0°, whereas this contrast is basically inverted for 41.4°. All bundles appear homogeneously grey at 66.6° with the intermediate carbon layers showing up as horizontal lines, indicating that all fiber bundle orientations are similar with respect to the grating bars. Since all the sheets feature a cross-woven pattern of the fiber bundles these contrast variations repeat after 90°, 180°, 270° and 360° sample rotation. Note that block (3) does however not display a visible DFC signal of the bundles for 90° and 270° where the structure is projected along the long axis of the block, whereas DFC signal is extraordinarily clear for 0° and 180°. While block (1) behaves similar to block (3), block (2) hardly shows any DFC signal corresponding to the fiber bundles orientation. Altogether 601 DFC projections were recorded, which were then in turn used to
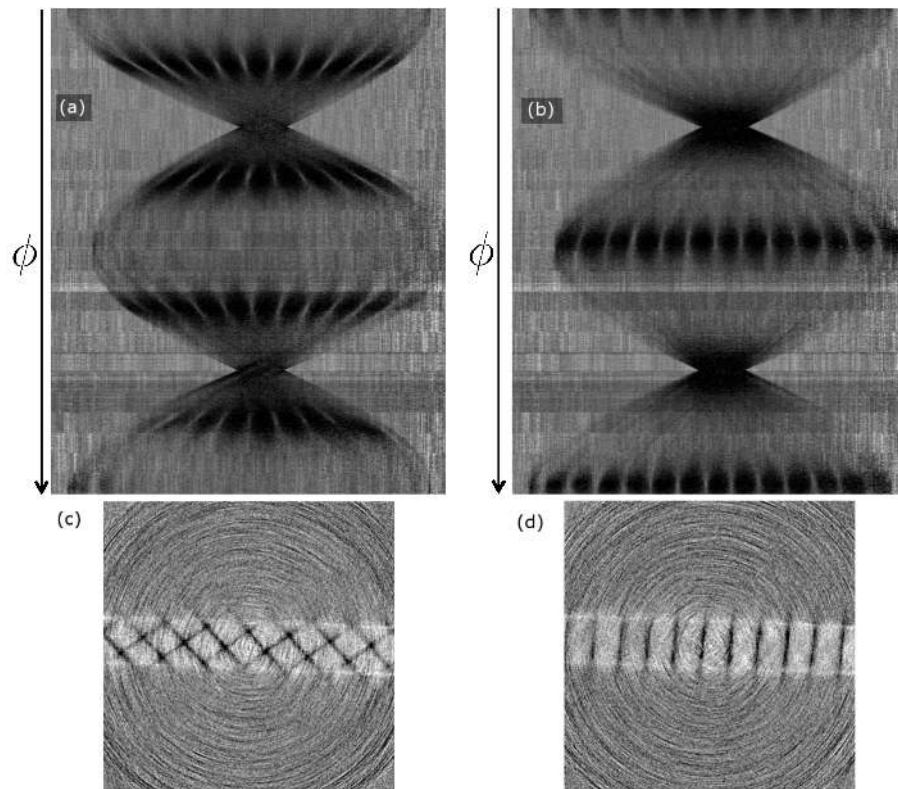

Fig. 6. Dark-field sinograms of the CFRC block, corresponding to the horizontal image line indicated by the white arrows in Fig. 5(b): (a) refers to the upper, (b) to the lower image line. The vertical axis represents the projection angle ϕ. "Dark spots" correspond to maximum alignment of the fiber bundles with the grating bars. (c, d) Reconstructed slices from the sinograms in (a,b). Bright intensities correspond to carbon fiber bundles, black corresponds to the carbon matrix in between the bundles. Note the clear difference in fiber bundle orientation in different slices.

reconstruct a three-dimensional volume of the sample scattering power by standard filtered back-projection (using the iRadon function in Matlab, Mathworks Inc., US). Figures 6(a) and (b) show two representative sinograms (corresponding to the horizontal image lines indicated by the white arrows in Fig. 5(b) along with the reconstructed dark-field CT slices of the same vertical positions (Figs. 6(c) and (d)). Note that, at specific projection angles, where the bundles mostly align with the grating bars, the sinograms show dark spots, indicating that the local orientation of these fiber bundles in that selected plane has a maximum scattering power for these values of ϕ. The anisotropy of the dark-field contrast appears as bright and dark patterns in the reconstructed slices (FBP involves taking the negative logarithm of the data, thus also inverting the image contrast) which are either diagonal crossed interweaved fiber bundles (Fig. 6(c)) or parallel cross-woven bundles (Fig. 6(d)). Note that only the bundles parallel to the short axis of the sample are reconstructed, whereas no distinctive patterns are observed parallel to the long sample axis. The carbon matrix in between the bundles appears black in the reconstructed slices. Note that CFRC sample (3) has a bar-like shape and has therefore a very anisotropic thickness, which shows up in the tailored shape of the sinograms. The filtered back-projection corrects for these thickness effects by redistributing the scattering power into the original shape of the sample (cf. Figs. 6(c) and (d)).

3.2. Single carbon fiber bundle

As one can see from Fig. 5, the impact of the projection angle on the dark-field contrast has to be considered. Therefore a carbon fiber stack with defined fiber orientation was used for a DFC analysis, in which the signal was averaged over a region of interest (ROI) corresponding to the sample overlap for all 20 recorded azimuthal angles ϕ from $0°$ to $342°$ (cf. Fig. 4). Note that aligning the fiber bundle with the grating bars ($\theta = 0°$) yields low visibility and no azimuthal variations in the DFC signal and is therefore not shown in this study.

For comparison, Fig. 7 shows two series of DFC images for two different elevation angles: $15°$ (Fig. 7(a)) and $60°$ (Fig. 7(b)). The six images shown for each elevation correspond to the first six azimuthal angles: $0°, 18°, 36°, 54°, 72°$ and $90°$. One can readily see that the DFC signal, i.e. the normalized visibility is minimum (darkest) for $\phi = 0°$ for both elevations (top) and decreases, i.e. becomes brighter with increasing azimuthal angle until $\phi = 90°$ (bottom). The changes in DFC, i.e. the span between darkest and brightest fiber contrast becomes visibly stronger for $\theta = 60°$ compared to the lower elevation of $\theta = 15°$. Note, that the ROI for DFC signal averaging corresponds to the overlap of the fibers in all azimuthal steps and has to be adapted for each elevation angle. Figure 8 shows this averaged DFC signal $\frac{V}{V_0}$ as a function of the azimuthal angle ϕ for the four measured sample elevations $\theta = 30°, 45°, 45°$ and $90°$. As expected, all DFC curves show periodic modulations with $180°$ repeat. For the bundle elevations up to $60°$, the DFC signal appears to be well modeled by a $\sin^2$-function, with higher amplitudes for larger elevation angles. The DFC for $90°$ fiber elevation angle, as it is present in the measurement of the CFRC sample (cf. Fig. 5), differs significantly. For $\theta = 90°$ the DFC signal rises quickly from zero to almost unity, where it maintains a plateau and drops back sharply to almost zero for $\phi = 180°$. This behavior can be readily explained: the fiber bundle oriented parallel to the X-ray propagation (maximum scattering sensitivity of the setup), and the fiber bundle has an orientation perpendicular to the grating bars and X-ray propagation (minimum scattering sensitivity).

The scattering power for the fiber stack oriented nearly parallel to the X-ray propagation ($\phi = 0°$ or $180°$) is maximum because of the strong scattering along the stack, whereas it is minimum for the opposite orientation. For the latter the X-rays for larger elevations are scattered mainly parallel to the grating bars, and the interferometer is insensitive for this particular scattering direction. For smaller sample elevations, the DFC signal modulations flatten out and appear
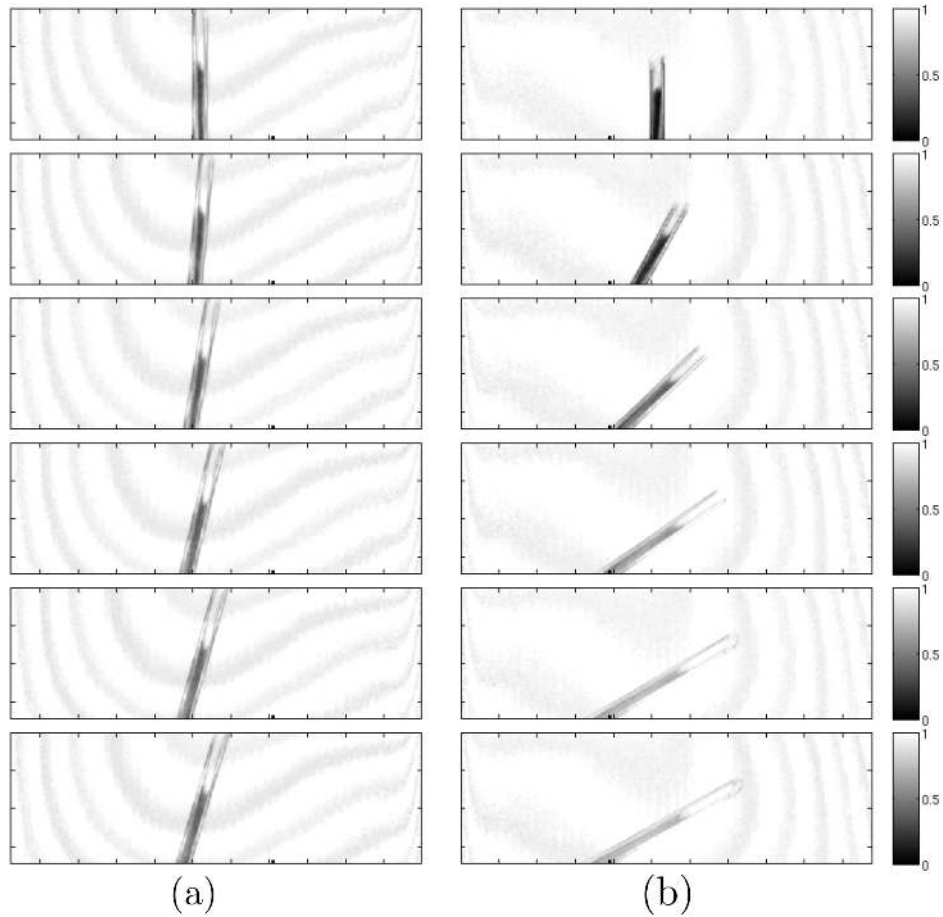
Fig. 7. DFC images of the fiber capillary for elevation angles $\theta = 15°$ (a) and $\theta = 60°$ (b). Each column shows a series of six dark-field images obtained at the azimuthal angles $\phi = 0°, 18°, 36°, 54°, 72°$ and $90°$ (from top to bottom). Minor Moiré patterns are visible in the images.

to converge towards a constant value of ~ 0.3 for θ close to $0°$. The functional dependence, i.e. the scattering power of the fiber bundle, when rotated in 3D has been further studied by fitting sinusoidal functions to the measured values, described (according to [9] and [11]) by the following formula:

$$\widetilde{DFC}(\phi) = -\ln(DFC(\phi)) = \alpha + \beta \cdot \sin^2(\phi) \qquad (2)$$

α is known to represent the fraction of the X-ray beam's isotropic contribution to scattering, and β the anisotropic scattering power of a fiber (or volume element of the fiber bundle, respectively). To correct for the varying effective thickness of the cylindrical fiber sample transmitted by the beam when rotating with the azimuthal angle, the conjugate diameter of the elliptical shape when tilting the cylindrical capillary has to be considered by

$$d_{eff}(\phi) = \frac{r_{min} r_{max}}{\sqrt{r_{min}^2 \cos^2(\phi) + r_{max}^2 \sin^2(\phi)}}. \qquad (3)$$
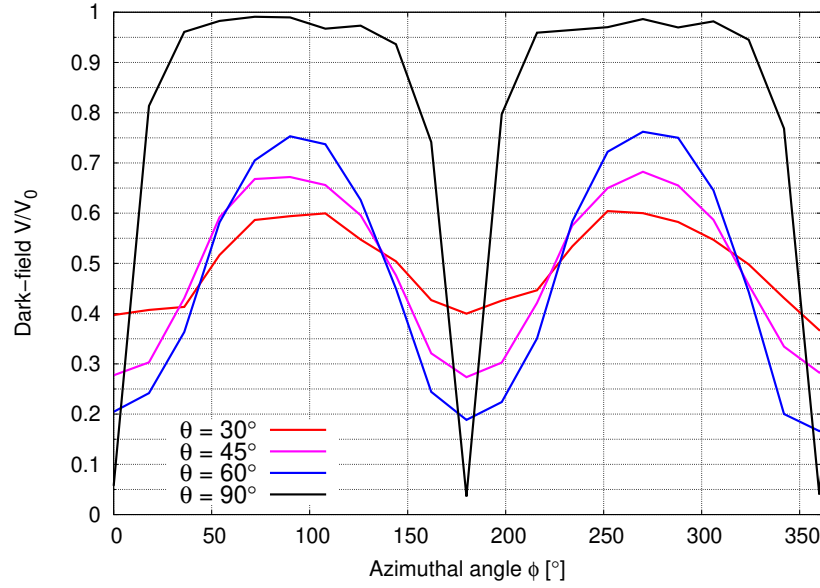
Fig. 8. Dark-field signal of the stacked fiber bundle, averaged over a region of interest as exemplary shown in Fig. 4. Each curve corresponds to a different sample elevation $\theta = 30°, 45°, 60°$ and $90°$ with respect to the grating bars. The azimuthal angle varies between $0°$ and $360°$ ($18°$ steps).

r_{min} and r_{max} denote the half-axes of the ellipse, r_{min} is the radius of the circular fiber bundle and r_{max} is its maximum enlargement, which is $r_{max} = \frac{r_{min}}{\cos(\theta)}$. Therefore the traversed thickness calculates to

$$d_{eff}(\phi, \theta) = \frac{r_{min}}{\sqrt{\sin^2(\phi) + \cos^2(\phi)\cos^2(\theta)}}. \tag{4}$$

$\theta = 90°$ represents a limiting case, Eq. (4) can hence not be applied for that case, which is available for the measurement of the CFRC sample object.

An exponential attenuation law can be assumed for the DFC signal, whereby the normalized visibility signal decreases exponentially with the thickness of the sample. The exponent is an extinction coefficient, comparable to the linear intensity coefficient in conventional attenuation imaging, and directly related to material properties. To refer the scattering coefficients α and β directly to that extinction coefficient, the DFC values have to be multiplied with the angle-dependent factor $\sqrt{\sin^2(\phi) + \cos^2(\phi)\cos^2(\theta)}$ to include rotation influence. Therefore we exploit the corrected DFC values using the function

$$-\ln(DFC_{measured}(\phi, \theta)) \cdot \sqrt{\sin^2(\phi) + \cos^2(\phi)\cos^2(\theta)} = \alpha_{corr} + \beta_{corr} \cdot \sin^2(\phi) \tag{5}$$

The results of the fitting for the elevation angles $\theta = 30°, 45°$ and $60°$ are summarized in Table 1. We find that the isotropic component α_{corr} is decreasing with larger elevation angles. Therefore, the larger the elevation, the stronger the DFC signal is dominated by the anisotropic part. The scattering power β_{corr} is increasing with higher elevation angle from 0.316 to 0.629. Note that β_{corr} is an elevation-dependent scattering value that includes the influence of the angle θ. To obtain the total anisotropic scattering power β, β_{corr} has to be divided by $\sin(\theta)$, respectively. For the investigated carbon fiber specimen we hereby obtain an anisotropic scattering

Table 1. Results of the $\sin^2(\phi)$-fit to the corrected logarithmic dark-field values according
to Eq. (5), taking into account the effective thickness of the sample.

Elevation θ [°]	α_{corr}	β_{corr}	RMSE
30	0.488	0.316	0.0331
45	0.343	0.547	0.0408
60	0.239	0.629	0.0476

power β of 0.710 ± 0.042. As one can easily deduce from the increasing RMSE-values for the fit, the lower the elevation, the better the DFC curve, corrected for thickness, corresponds to the assumed $\sin^2(\phi)$-function. This is why we assume further influences due to the different geometrical shape of the sample at high elevations, as previously described in [8].

4. Discussion

From the study of the DFC signal from a single bundle of carbon fibers, which was used to approximate a fiber bundle as present in woven fabric in CFRC materials, we could estimate and describe the scattering power, i.e. the resulting DFC signal, as a function of both the azimuthal angle and the fiber elevation with respect to the grating bars. For the scattered radiation we confirmed and quantified a $\sin^2$-like behavior for the azimuthal angle in the polar angle range from $30° - 60°$. For higher elevations the sinusoidal shape gets reproduced slightly worse, why we consider the carbon fiber stack changing its projective representation from line to spherical shape, which confirms the non-analytical behavior which is frequently observed in DFC images of ordered structures [8]. The azimuthal scan for the bundle oriented perpendicular to the grating bars is characterized by a somehow bimodal DFC signal: the normalized visibility was found constant and almost unity around $\phi = 90°$ and $270°$ as there is no sensitivity of the setup to structures aligned perpendicular to the grating bars, whereas it droppes sharply to almost zero at $\phi = 0°, 180°$ and $360°$. This effect is explained by the parallel orientation of the fibers with the direction of X-ray propagation at these angles. The periodic behavior of the DFC signal during axial scanning further affirms the symmetry of the grating setup and measurement reliability. In order to quantify the scattering power of the fibers, we assume an exponential thickness-contrast law, in analogy to attenuation images. The DFC is corrected for the projected thickness of the inclined fiber stack. This exponential law was further confirmed when 3D volume DFC images were reconstructed by standard FBP from an anisotropic bulk scattering object, namely a block of CFRC material. The FBP does not only yield a reasonable reconstruction of the scattering density and corrected for the overall anisotropic shape of the sample, but also provides direct visual impression of the cross-woven fiber bundles sheets. We therefore project, that DFC tomography has a very high potential, based on the extraction of the dark-field extinction coefficient, for the study of materials whose fiber orientation is of interest, providing an adapted reconstruction algorithm incorporates multiple tomography datasets. Note that we chose a CFRC laminate consisting solely of carbon components. Therefore in the attenuation image low contrast is achievable between carbon fiber bundles and the embedding graphite matrix, in contrast to the presented dark-field images in which the influence of oriented micro-fibers enhances the visibility of the structural consistency. The sample contained only sheets with fiber bundle orientations in the horizontal plane, hence perpendicular to the grating bars, thereby excluding the possibility of bundles with elevation angles non-zero which in reality would be the common case. Reconstruction kernels facilitating the integration of the azimuthal dark-field contrast with its periodicity of $180°$ for tomographic scans along $360°$ have therefore to be developed. Yet, studying natural fiber composite materials, like bones or wood should be directly feasible with this technique.

5. Conclusion

Phase-contrast imaging based on the Talbot-Lau grating interferometer is a multi-contrast technique with a lot of potential applications in non-destructive testing of materials as well as in medical imaging. In addition to attenuation contrast, it provides differential phase-contrast and dark-field contrast images. The DFC signal, calculated from the normalized visibility $\frac{V}{V_0}$, encodes scattering information of specimen structures well below pixel resolution, which are of a special interest to examinations on material structure focusing on fiber orientations. The application of standard FBP reconstruction to DFC projections led to an incomplete representation of the structure. Despite the direct visual access, which these reconstructions have been shown to provide on the fiber bundle weave patterns, it has to be noted that more adapted reconstruction algorithms (e.g. based on algebraic techniques), could combine DFC and absorption signals, possibly from multiple datasets from scans with different rotation axes, and yield far more accurate results on the local fiber orientation of the structure. By analyzing the DFC signal for a simple carbon fiber bundle we were able to reveal its angular dependence with respect to the elevation θ, at least for fiber elevations up to $60°$. Thus, the possibility to analyze the ordered microstructures of anisotropic materials, including their local fiber orientation, is readily at hand. Our data from the simple fiber bundle could thereby serve as an input to develop a dedicated algebraic tomography reconstruction for X-ray dark-field imaging of higly ordered materials. The technical requirements which are necessary to perform such an analysis do not go beyond the conventional X-ray tube setup, and is therefore relatively simple to operate, given the additional gratings.